Supplementary Information for

Ultrafast heat transfer in single palladium nanocrystals seen with an X-ray free-electron laser

David Yang[1*], James Wrigley[2], Jack Griffiths[1], Longlong Wu[1†], Ana F. Suzana[1‡], Jiecheng Diao[3§], Angel Rodriguez-Fernandez[2], Joerg Hallmann[2], Alexey Zozulya[2], Ulrike Boesenberg[2], Roman Shayduk[2], Jan-Etienne Pudell[2], Anders Madsen[2], Ian K. Robinson[1,3*]

[1]Condensed Matter Physics and Materials Science Department, Brookhaven National Laboratory, Upton, NY, 11973, United States.

[2]European X-Ray Free-Electron Laser Facility, Holzkoppel 4, 22869 Schenefeld, Germany.

[3]London Centre for Nanotechnology, University College London, London, WC1E 6BT, United Kingdom.

[†]Present address: Shanghai Advanced Research Institute, Chinese Academy of Sciences, Shanghai, 201210, China

[‡]Present address: Chemical Sciences and Engineering Division, Argonne National Laboratory, Lemont, IL, 60439, United States.

[§]Present address: Center for Transformative Science, ShanghaiTech University, Shanghai, 201210, China

[*]Corresponding author. Email: dyang2@bnl.gov, i.robinson@ucl.ac.uk

This PDF file includes:

Supplementary Notes 1 to 3

Supplementary Figures 1 to 13

Supplementary Tables 1 and 3

Supplementary Notes

1 Peak oscillation fitting

The oscillations in horizontal peak position in Fig. 3a were fitted using an empirical damped sinusoidal function with amplitude modulation at the troughs, shown in Eq. 1,

$$\begin{aligned} s(\tau) &= A_1 \cos\left(\frac{2\pi\tau}{T_1} + \phi_1\right) \\ S_p(\tau) &= \left[A_1 + \text{rectifier}(s(\tau)) \cdot A_2 \cos\left(\frac{2\pi\tau}{T_2} + \phi_2\right)\right] \cdot e^{-\lambda\tau} + C, \text{ where} \\ \text{rectifier}(s(\tau)) &= \begin{cases} 1 & \text{if } s(\tau) < 0, \\ 0 & \text{otherwise, and} \end{cases} \end{aligned} \tag{1}$$

where τ is the delay time, A_1 and A_2 are the amplitudes, T_1 and T_2 are the periods, ϕ_1 and ϕ_2 are the phase shifts, λ is the damping constant, and C is the offset. The subscripts 1 and 2 refer to the variables for the signal and modifier, respectively. The fit parameters are shown in Table 1.

The oscillations of the FWHM of the fitted Bragg peak for crystal A are captured in Fig. 3 d. These oscillations are fitted with a damped sinusoidal function, shown in Eq. 2,

$$S_w(\tau) = B \cos\left(\frac{2\pi\tau}{P} + \beta\right) e^{-\zeta\tau} + D, \tag{2}$$

where B is the amplitude, P is the period, β is the phase shift, ζ is the damping constant, and D is the offset. The fit parameters are shown in Table 2.

2 Crystal rotation

The rotation for crystal A with respect to the rocking axis is estimated in Fig. 7. The measured rocking curve of the diffraction peak is a direct measure of how rapidly the intensity drops off with angle. When there is a change in average lattice parameter, there will be a deviation of Bragg angle, $\Delta\theta$. The theta deviation for 170 mJ/cm^2 in Fig. 7b is ≈ 0.035 ° at around 40 ps. The theta angle for the Pd 111 reflection is 17.9 °. Thus, the expected ΔQ for this deviation is determined by,

$$\begin{aligned}\Delta Q &= \frac{4\pi}{\lambda}\left[\sin\left(\theta - \Delta\theta\right) - \sin\left(\theta\right)\right] \\ \Delta Q &= \frac{4\pi}{1.377602\ \mathring{\mathrm{A}}}\left[\sin\left(17.9\ ^\circ - 0.035\ ^\circ\right) - \sin\left(17.9\ ^\circ\right)\right] \\ \Delta Q &= 0.0053\ \mathring{\mathrm{A}}^{-1}\end{aligned} \tag{3}$$

At negative delay time in Fig. 3a, $Q_0 = 2.8038\ \mathring{\mathrm{A}}^{-1}$. Thus, $Q_0 - \Delta Q = 2.7985\ \mathring{\mathrm{A}}^{-1}$, which agrees with Q at around 40 ps in Fig. 3a.

For 230 mJ/cm^2 in Fig. 7b, $\Delta\theta \approx 0.050\ ^\circ$ at around 40 ps. Thus, the expected ΔQ for this deviation is determined by,

$$\begin{aligned}\Delta Q &= \frac{4\pi}{\lambda}\left[\sin\left(\theta - \Delta\theta\right) - \sin\left(\theta\right)\right] \\ \Delta Q &= \frac{4\pi}{1.377602\ \mathring{\mathrm{A}}}\left[\sin\left(17.9\ ^\circ - 0.050\ ^\circ\right) - \sin\left(17.9\ ^\circ\right)\right] \\ \Delta Q &= 0.0076\ \mathring{\mathrm{A}}^{-1}\end{aligned} \tag{4}$$

At negative delay time in Fig. 3a, $Q_0 = 2.8038\ \mathring{\mathrm{A}}^{-1}$. Thus, $Q_0 - \Delta Q = 2.7962\ \mathring{\mathrm{A}}^{-1}$, which is reasonably expected for 230 mJ/cm^2 at around 40 ps in Fig. 3a. Thus, the rotation at high laser fluences can be explained as due to the average lattice expanding and contracting. This noticeably changes the intensity of the Bragg peak of crystal A at 170 mJ/cm^2 and 230 mJ/cm^2.

3 Two-temperature model simulation

The simulations were performed using a one-dimensional (1D) TTM simulation using the `udkm1Dsim` toolbox [1]. The crystal is approximated as a 1D slab with a thickness of 180 nm, initial temperature of 298 K, and thermally insulated surfaces. An 800 nm laser with a pulse width of 15 fs and fluence of 1 mJ/cm^2 for Pd and 70 mJ/cm^2 for Au (chosen to match the experimental strain magnitudes) reaches the surface at 0 ps. The values used for the simulation are shown in Table 3.

To capture the non-equilibrium heating and subsequent lattice dynamics as a function of depth, z, below the surface and delay time, we present maps of the electron temperature (T_e), lattice temperature (T_l), and strain along the depth of the slab (ε_{zz}) in Fig. 12. The simulations were performed for Pd and Au to highlight how our findings differ from previous work on Au microcrystals [2, 3].

In the first few picoseconds for Pd, we observe hot electrons penetrate partway through the slab, shown in Fig. 12a. The hot electrons couple to the lattice, which gets rapidly heated in the first few nanometres below the surface, shown in Fig. 12b. This launches a sharp bipolar strain wave that travels through the crystal at the speed of sound, shown in Fig. 12c. This inhomogeneous strain has a compressive and expansive component, leading to the splitting of the Bragg peak, shown in Fig. 13a and our experimental data in Fig. 2.

In the first few picoseconds for Au, we observe hot electrons penetrate deeply into the slab, shown in Fig. 12d. This allows the slab to be heated relatively more uniformly in Au compared to Pd, shown in Fig. 12e. The hot electrons in Au have a weaker coupling to the lattice, due to the lower electron-phonon coupling [4], thus the increase in T_l is not as high compared to that of Pd. This launches a relatively homogeneous strain wave that travels through the crystal at the speed of sound, shown in Fig. 12c. This acoustic wave has negligible compression, leading to a simple oscillation of the Bragg peak, shown in Fig. 13f, which has been observed in similar experiments [2, 3].

Supplementary Figures

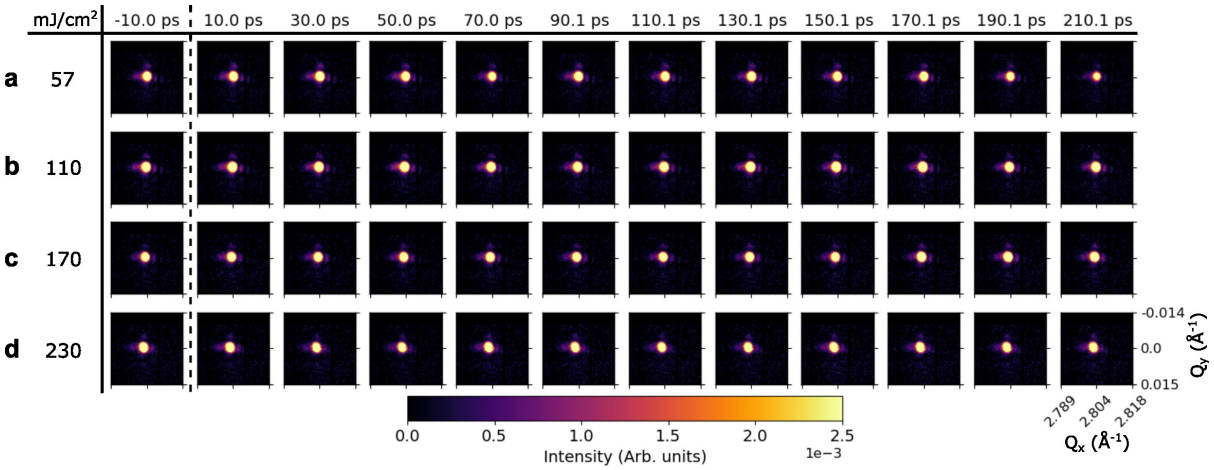

Supplementary Figure 1: The unpumped pulses of the 111 Bragg peak intensity on a linear scale for crystal A at various delay times and laser fluences. Rows **a** - **d** correspond to sequential delay measurements using different fluences.

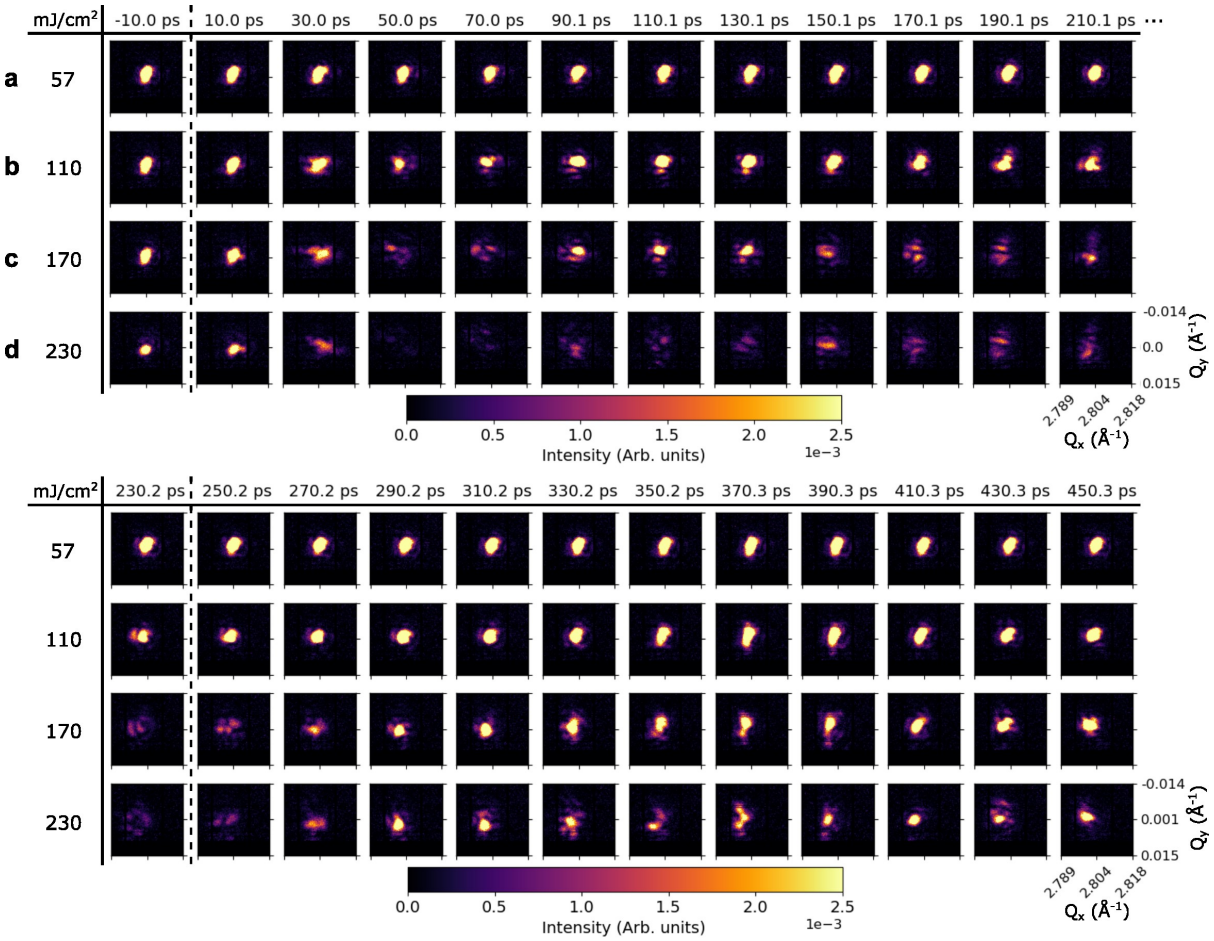

Supplementary Figure 2: Evolution of the 111 Bragg peak intensity on a linear scale for crystal B at various delay times and laser fluences. Rows **a** - **d** correspond to sequential delay measurements using different fluences.

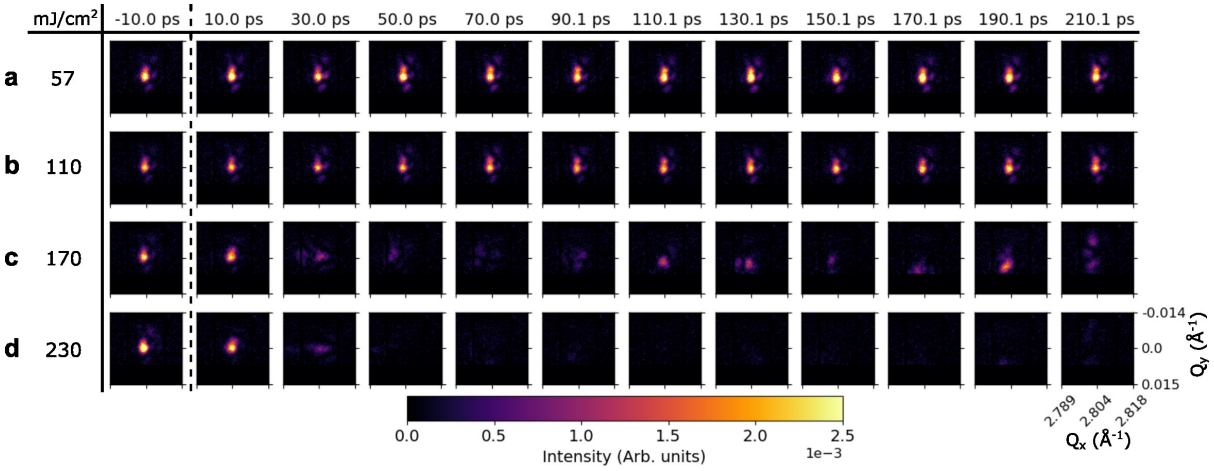

Supplementary Figure 3: Evolution of the 111 Bragg peak intensity on a linear scale for crystal C-1 at various delay times and laser fluences. Rows **a** - **d** correspond to sequential delay measurements using different fluences.

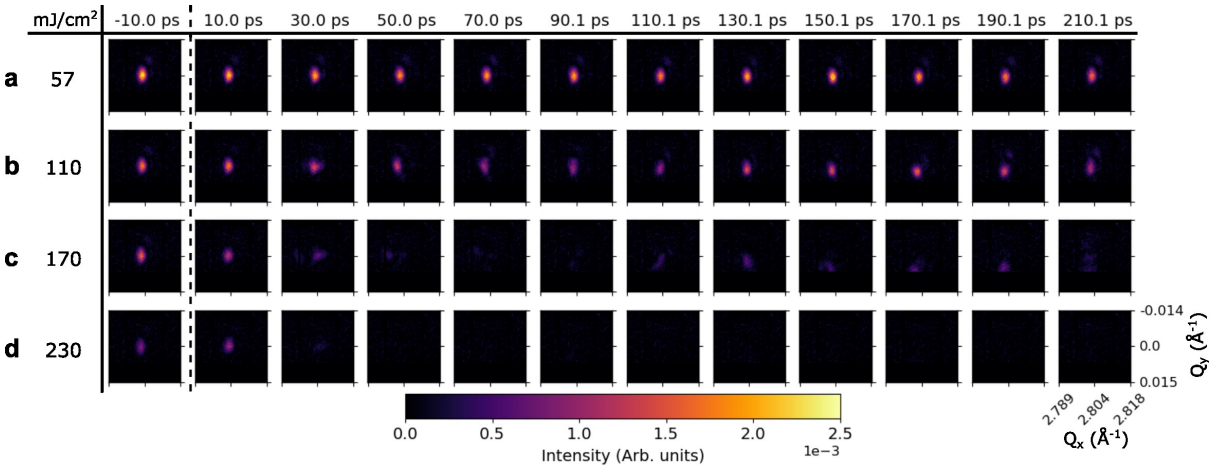

Supplementary Figure 4: Evolution of the 111 Bragg peak intensity for on a linear scale crystal C-2 at various delay times and laser fluences. Rows **a** - **d** correspond to sequential delay measurements using different fluences.

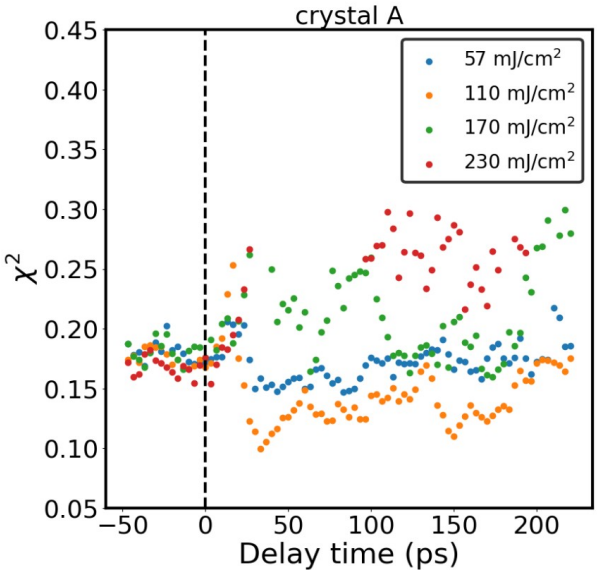

Supplementary Figure 5: The χ^2 error of the Gaussian fit of the Bragg peak at various delay times and laser fluences. Each point corresponds to the fits shown in Fig. 3a and 6a.

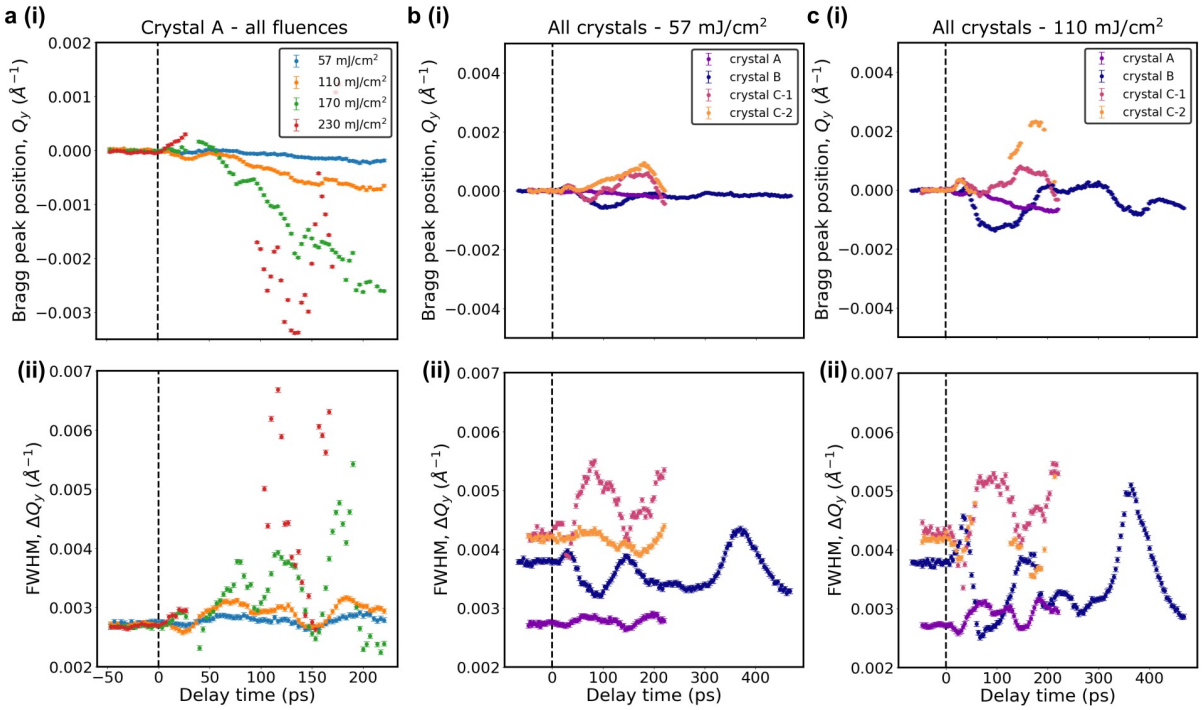

Supplementary Figure 6: Summary of the changes to the Gaussian-fitted Bragg peaks along the Q_y (vertical) detector direction as a function of laser fluence and delay time. **a** Crystal A's fitted parameters for various laser fluences. (i) Fitted position of the Bragg peak along Q_y. The oscillations were fitted with Eq. 1 for all fluences except for 230 mJ/cm^2 due to a lack of signal. (ii) Fitted FWHM of the Bragg peak along Q_y. The oscillations were fitted with Eq. 2. **b** Fitted parameters for a laser fluence of 57 mJ/cm^2 on all measured crystals. **c** Fitted parameters for a laser fluence of 110 mJ/cm^2 on all measured crystals. Crystal C-1 and C-2 are two successive measurements on the same crystal. The error bars reflect two standard deviations of repeated measurements at negative delay times. The error of the Gaussian fits is shown in Fig. 9 for **b** and **c**. The equivalent of this figure in the Q_x direction is Fig. 3.

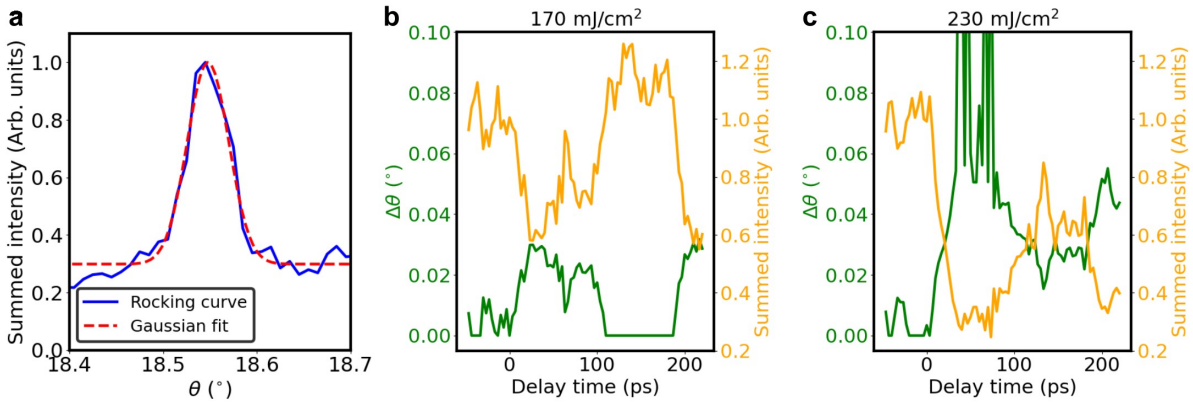

Supplementary Figure 7: Estimation of rotation around the θ rocking axis for crystal A at high laser fluences based on the normalised summed intensity of the Bragg peak cropped to a 64×64 array. **a** The rocking curve for crystal A with a fitted Gaussian function used to compute the magnitude of θ rotation. **b** The rotation, given by theta deviation, $\Delta\theta$, for 170 mJ/cm^2. **c** The rotation for 230 mJ/cm^2. The summed intensity for **b** and **c** is normalised to the average summed intensity at negative delay times.

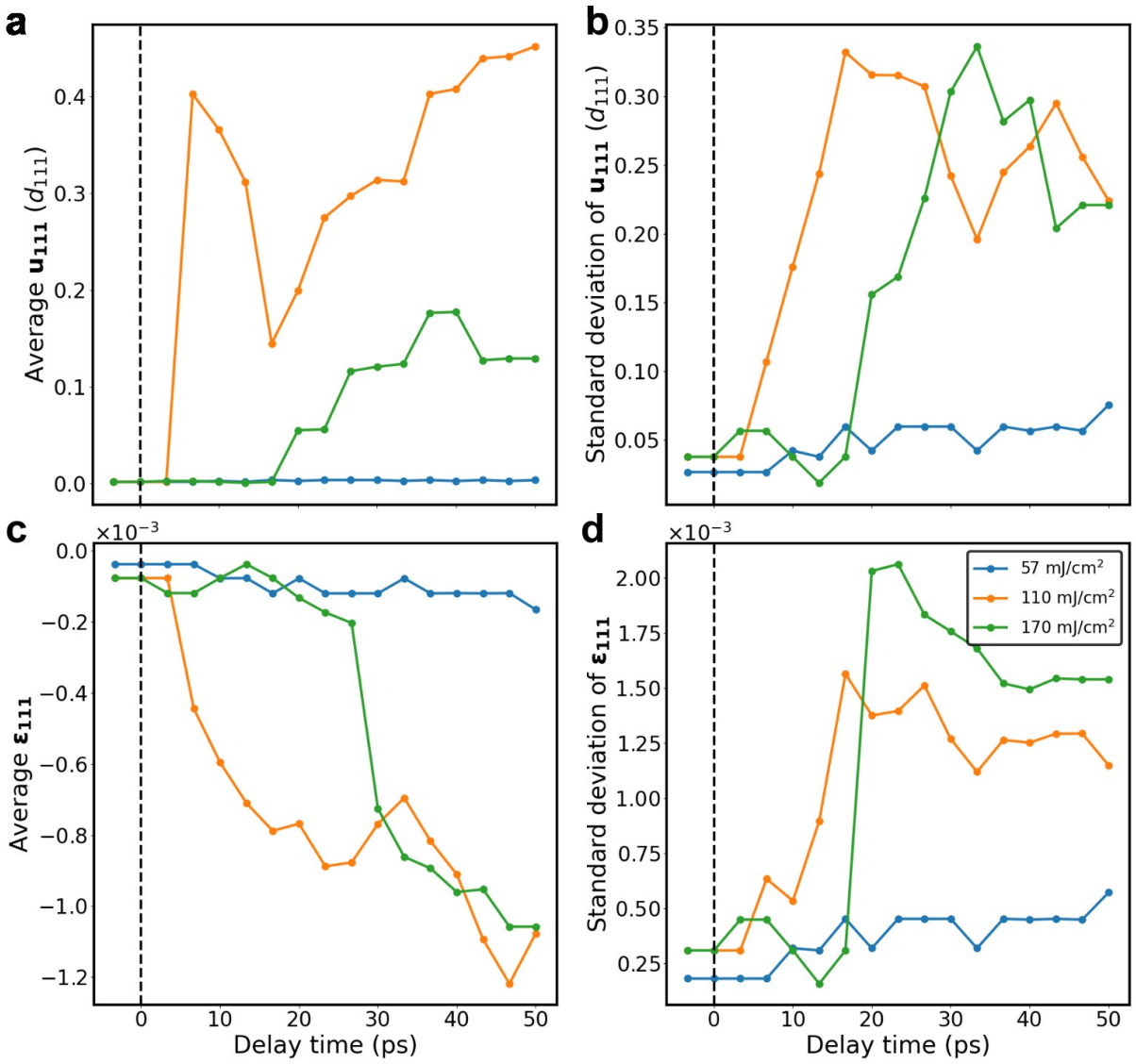

Supplementary Figure 8: Additional displacement and strain trends for the 2D model of crystal A in Fig. 4. Displacement trends are shown for **a**, the mean $\mathbf{u_{111}}$, and **b**, the standard deviation of $\mathbf{u_{111}}$. Strain trends are shown for **c**, the mean ε_{111}, and **d**, the standard deviation of ε_{111}.

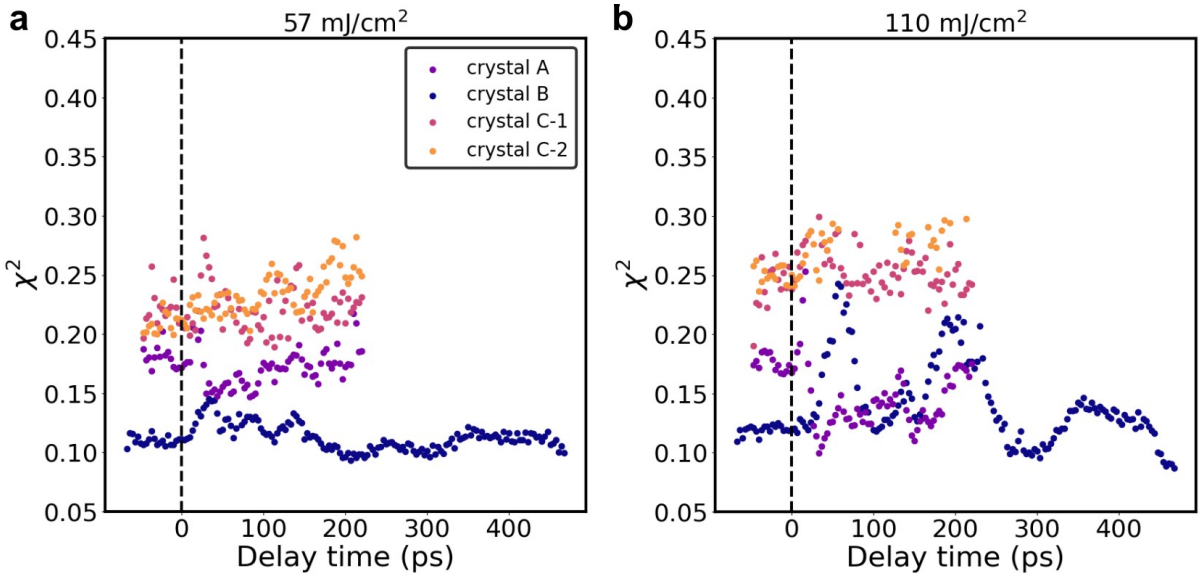

Supplementary Figure 9: The χ^2 error of the Gaussian fit of the Bragg peak for multiple crystals at various delay times for **a** 57 mJ/cm^2 and **b** 110 mJ/cm^2. Each point corresponds to the fits shown in Figs. 3b and c and 6b and c.

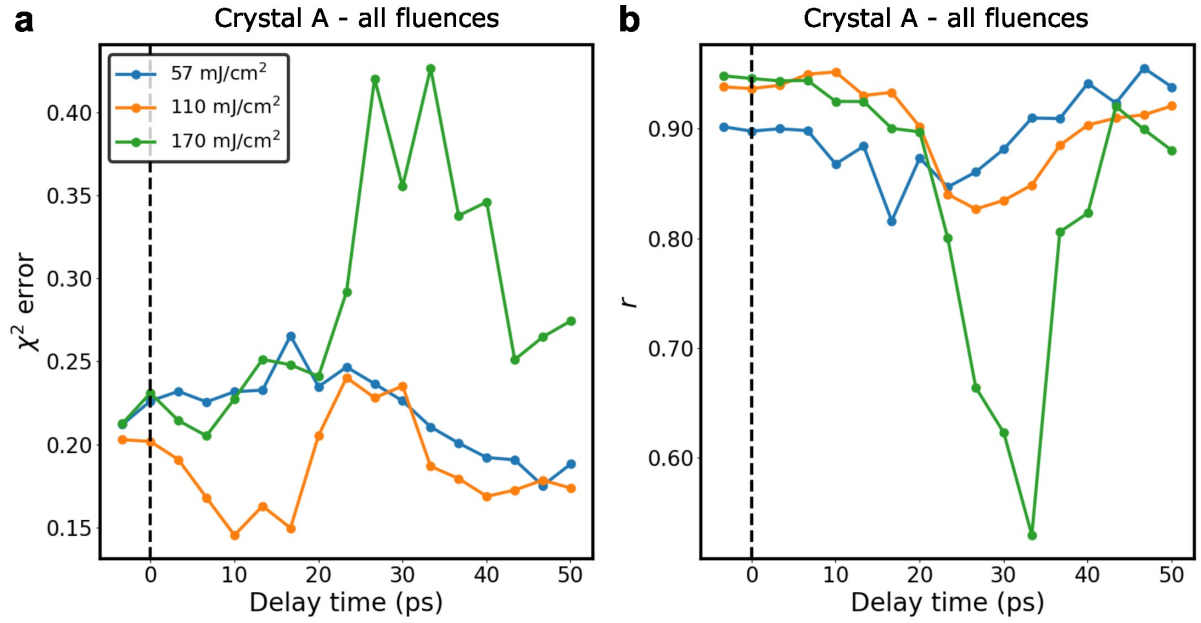

Supplementary Figure 10: Comparison between the normalised Bragg peak of the crystal A model compared to the normalised experimental Bragg peak in Fig. 4. **a** The χ^2 error. **b** The Pearson correlation coefficient, r.

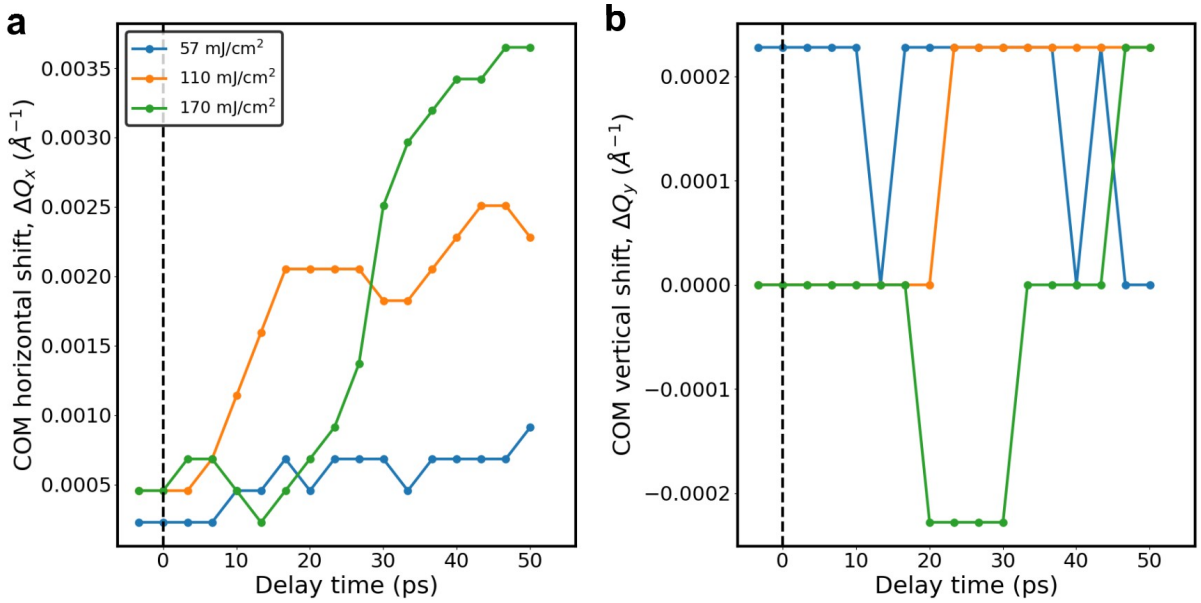

Supplementary Figure 11: Additional centre of mass (COM) parameters used for the crystal A model in Fig. 4. These COM shifts of the model Bragg peaks were implemented separately and are shown for both **a**, the horizontal direction, ΔQ_x, and **b**, the vertical direction, ΔQ_y.

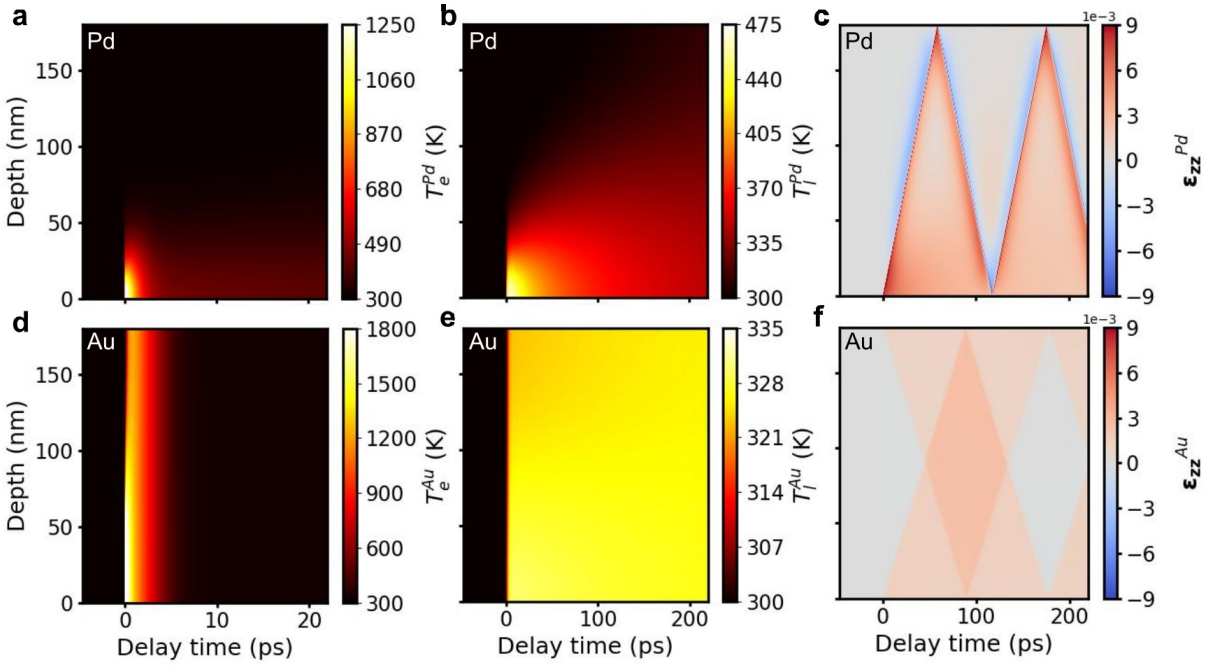

Supplementary Figure 12: A 1D TTM simulation of Pd compared to Au. The top row shows **a** the electron temperature (T_e), **b** the lattice temperature (T_l), and **c** strain along the depth of the crystal (ε_{zz}) for Pd. The bottom row shows **d** the electron temperature, **e** the lattice temperature, and **f** strain along the depth of the crystal for Au.

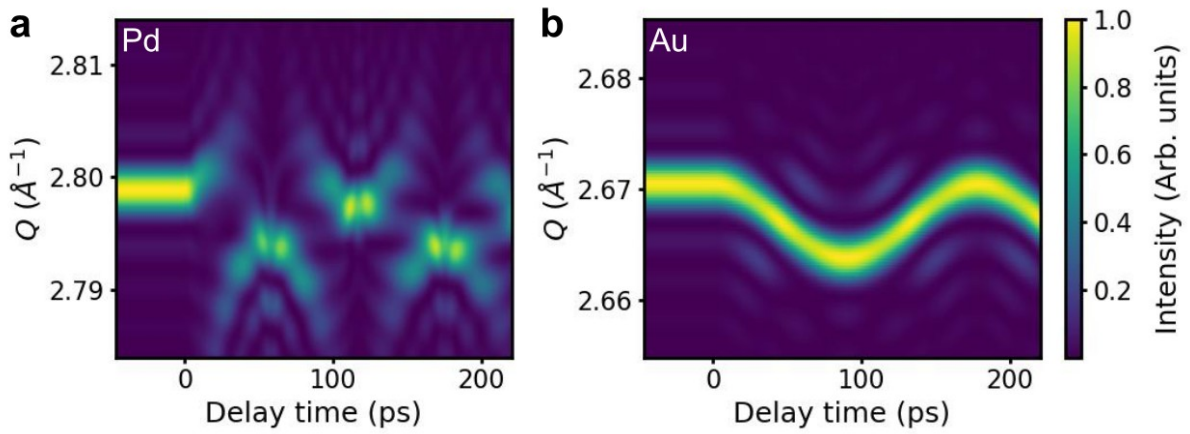

Supplementary Figure 13: A 1D dynamical X-ray diffraction simulation of the TTM for **a** Pd and **b** Au. For Pd, a splitting of the Bragg peak is observed, whereas Au shows a single Bragg peak.

Supplementary Tables

Supplementary Table 1: Eq. 1 fitted parameters for Fig. 3a

mJ/cm^2	A_1	T_1	ϕ_1	A_2	T_2	ϕ_2	λ	C
57	2.5×10^{-2}	122	-9.9×10^{-2}	1.4×10^{-2}	61	-3.0	6.1×10^{-3}	2.8
110	4.9×10^{-2}	120	3.6×10^{-1}	3.0×10^{-2}	61	-2.7	1.1×10^{-2}	2.8
170	8.5×10^{-2}	120	1.3×10^{-1}	-5.0×10^{-2}	61	-6.0	1.1×10^{-2}	2.8

Supplementary Table 2: Eq. 2 fitted parameters for Fig. 3d

mJ/cm^2	B	P	β	ζ	D
57	-9.4×10^{-4}	57	8.1×10^{-1}	1.9×10^{-2}	2.7×10^{-3}
110	-7.1×10^{-4}	58	1	0	3.5×10^{-3}
170	4×10^{-3}	58	1	0	7×10^{-3}

Supplementary Table 3: Numerical values used in the TTM simulations via the `udkm1Dsim` [1] toolbox.

Parameter	Pd value	Au value	Units	Description and Reference
ρ	1.2×10^4	1.93×10^4	kg/m^3	Density [5]
a_0	3.890	4.078	Å	Lattice constant [5]
c_S	3070	2030	m/s	Speed of sound [6, 5]
G	5×10^{17}	3×10^{16}	W/(m^3 K)	Electron–phonon coupling constant [4]
C_{ph}	238	129	J/(kg K)	Phonon heat capacity [5]
C_e	$0.088T_e$	$0.0034T_e$	J/(kg K)	Electron heat capacity [7, 8]
κ_{ph}	5	5	W/(m K)	Phonon thermal conductivity [9]
κ_e	$72 - 5$	$318 - 5$	W/(m K)	Electron thermal conductivity [9, 6]

Continued on next page

(continued)

Parameter	Pd Value	Au Value	Units	Description and Reference
Γ_{ph}	2.25	2.96	–	Phonon Grüneisen coefficient [10, 11]
Γ_e	2.22	1.6	–	Electron Grüneisen coefficient [10, 11]
B	180	166	GPa	Bulk modulus [5]
α_{ph}	$\Gamma_{ph}C_{ph}\rho/B$	$\Gamma_{ph}C_{ph}\rho/B$	K^{-1}	Phonon linear thermal expansion coefficient
α_e	$\Gamma_e C_e \rho/B$	$\Gamma_e C_e \rho/B$	K^{-1}	Electron linear thermal expansion coefficient
n	$2.02 + 5.09i$	$0.15 + 4.91i$	–	Complex refractive index at 800 nm [12]

References

[1] Daniel Schick. udkm1dsim – a python toolbox for simulating 1d ultrafast dynamics in condensed matter. *Computer Physics Communications*, 266:108031, 2021.

[2] J. N. Clark, L. Beitra, G. Xiong, A. Higginbotham, D. M. Fritz, H. T. Lemke, D. Zhu, M. Chollet, G. J. Williams, M. Messerschmidt, B. Abbey, R. J. Harder, A. M. Korsunsky, J. S. Wark, and I. K. Robinson. Ultrafast three-dimensional imaging of lattice dynamics in individual gold nanocrystals. *Science*, 341:56–59, 2013.

[3] Jesse N. Clark, Loren Beitra, Gang Xiong, David M. Fritz, Henrik T. Lemke, Diling Zhu, Matthieu Chollet, Garth J. Williams, Marc M. Messerschmidt, Brian Abbey, Ross J. Harder, Alexander M. Korsunsky, Justin S. Wark, David A. Reis, and Ian K. Robinson. Imaging transient melting of a nanocrystal using an x-ray laser. *Proceedings of the National Academy of Sciences of the United States of America*, 112:7444–7448, 2015.

[4] N Medvedev and I Milov. Electron-phonon coupling in metals at high electronic temperatures. *Physical Review B*, 102:64302, 8 2020.

[5] William M. Haynes, editor. *CRC Handbook of Chemistry and Physics, 93rd Edition*. CRC Press, 4 2016.

[6] G V Samsonov. *Handbook of the physicochemical properties of the elements*. Plenum Publishing Corporation, New York, 1968.

[7] J W Arblaster. Thermodynamic properties of gold. *Journal of Phase Equilibria and Diffusion*, 37:229–245, 2016.

[8] T Y Hsiang, J W Reister, H Weinstock, G W Crabtree, and J J Vuillemin. Magnetic field dependence of the electronic specific heat of palladium. *Physical Review Letters*, 47:523–526, 8 1981.

[9] M J Duggin. The thermal conductivities of aluminium and platinum. *Journal of Physics D: Applied Physics*, 3:L21, 1970.

[10] G K White and A T Pawlowicz. Thermal expansion of rhodium, iridium, and palladium at low temperatures. *Journal of Low Temperature Physics*, 2:631–639, 1970.

[11] K O McLean, C A Swenson, and C R Case. Thermal expansion of copper, silver, and gold below 30 k. *Journal of Low Temperature Physics*, 7:77–98, 1972.

[12] P B Johnson and R W Christy. Optical constants of transition metals: Ti, v, cr, mn, fe, co, ni, and pd. *Physical Review B*, 9:5056–5070, 6 1974.